The Effect of the Spin-Forbidden $CO(^1\Sigma^+) + O(^3P) \rightarrow CO_2(^1\Sigma_g^+)$ Recombination Reaction on Afterbody Heating of Mars Entry Vehicles

Lu T. Xu[1],

NASA Ames Research Center, Moffett Field, CA 94035
University of Illinois at Urbana-Champaign, Urbana, IL 61801

Richard L. Jaffe[2], David W. Schwenke[3]

NASA Ames Research Center, Moffett Field, CA 94035

and

Marco Panesi[4]

University of Illinois at Urbana-Champaign, Urbana, IL 61801

Vibrationally excited CO_2, formed by two-body recombination from $CO(^1\Sigma^+)$ and $O(^3P)$ in the wake behind spacecraft entering the Martian atmosphere, is believed to be responsible for the higher than anticipated radiative heating of the backshell, compared to pre-flight predictions. This process involves a spin-forbidden transition of the transient triplet CO_2 molecule to the longer-lived singlet. To accurately predict the singlet-triplet transition probability and estimate the thermal rate coefficient of the recombination reaction, *ab initio* methods were used to compute the first singlet and three lowest-energy triplet CO_2 potential energy surfaces and the spin-orbit coupling matrix elements between these states. Analytical fits to these four potential energy surfaces were generated for surface hopping trajectory calculations, using Tully's fewest switches surface hopping algorithm. Preliminary results for the trajectory calculations are presented. The calculated probability of a $CO(^1\Sigma^+) + O(^3P)$ collision leading to singlet CO_2 formation is on the order of 10^{-4}. The predicted flowfield conditions for various Mars entry scenarios predict temperatures in the range of 1000K-4000K and pressures in the range of 300-2500 Pa at the shoulder and in the wake, which is consistent with a heavy-particle collision frequency of 10^6 to 10^7 s^{-1}. Owing to this low collision frequency, it is likely that $CO_2(^1\Sigma_g^+)$ molecules formed by this mechanism will mostly be frozen in a highly nonequilibrium ro-vibrational energy state until they relax by photoemission.

I.   Introduction

In order to simulate the flowfield around a spacecraft and design efficient thermal protection system for entry into a planetary atmosphere, one needs to understand non-equilibrium chemical kinetics and radiation phenomena in hypersonic flows. Work is underway within NASA to develop a

---

[1] Postdoctoral Research Associate, Aerothermodynamics Branch, Mail Stop 230-3;
Department of Aerospace Engineering, University of Illinois at Urbana-Champaign, 104 S Wright St, Urbana, IL 61801. lu.xu@nasa.gov

[2] Senior Research Scientist, Aerothermodynamics Branch, Mail stop 230-3. Associate Fellow AIAA

[3] Senior Research Scientist, NAS Physics Branch, Mail Stop 258-2

[4] Assistant Professor, Department of Aerospace Engineering, University of Illinois at Urbana-Champaign, 306 Talbot Laboratory, 104 S Wright St, Urbana, IL 61801. Senior Member AIAA

non-equilibrium model based on *ab initio* computational chemistry that can be incorporated into computational fluid dynamics (CFD) simulations and lead to predictions of the convective and radiative heat fluxes experienced by the spacecraft. The chemical and physical processes encountered during high-speed Earth entry are fairly well understood, but the situation for Mars entry is much less so.

The Martian atmosphere is composed mostly of CO_2 (96% by volume), with some N_2 (1.9%) and Ar (1.9%) plus other minor constituents. [1] For most proposed NASA missions, the vehicle entry speeds will be 4–8 km/s and the equilibrium temperature of the bow shock layer will be 5,000–9,000 K. For 6-8 km/s entry, most of the CO_2 is rapidly dissociated in the shock layer, resulting in the formation of $CO(^1\Sigma^+)$ and $O(^3P)$. In this case, CO 4th-positive emission in the VUV is the major component in the radiative heat flux. However, for 4-5 km/s entry, hot CO_2 is also present in the shock layer and infrared emission from that molecule is an important contributor to the radiative heating. See Johnston and Brandis [2] for a discussion of the radiative heating. As the flow expands around the shoulder and into the backshell region of the spacecraft, the temperature and pressure drop, and recombination reactions are more probable. In this part of the flow, temperature will probably drop to 1,500-4,000K and pressure will drop from about 50,000 Pa in the bow shock layer to less than 3000 Pa. The radiative heat flux incident on the backshell is predominately infrared emission from CO_2 and CO. In practice, the Carbon Dioxide Spectroscopic Database (CDSD) [3] is used to predict the spectral intensity of this radiation. That model assumes the populations of the ro-vibrational levels of CO_2 are in thermal equilibrium, which is probably not accurate for expanding flows where relative internal energy populations become frozen as the temperature and pressure drop.

In general, the heat flux experienced by the forebody of the vehicle during atmospheric entry is much greater than that experienced by the afterbody. Consequently, the forebody heat flux has been studied to a much greater extent by flight instrumentation, CFD and ground-based experiments. However, a recent CFD study by da Silva and Beck [4] suggested that non-equilibrium CO_2 infrared radiation (IR) is the dominant contributor to the afterbody heating of Mars entry vehicles and this radiative heat flux is significantly greater than previously assumed. As a result, the requirements for backshell thermal protection for Mars entry are being reconsidered. More recent computational [5, 6, 7] results seem to support this conclusion. Two sets of expansion tube experiments [8, 9] are in general agreement with the CFD studies, but their results are not conclusive. These experiments, using fast CO_2 flows, have provided the first measurements of radiative heating in the expanding flow region behind small sphere-cone models. However, the expansion tube measurements were carried out for freestream velocities under 5 km/s and not much of the CO_2 in the flow was dissociated in the bow shock layer. Therefore, their relevance to higher speed entries is unclear.

The most widely used non-equilibrium chemistry model for describing Mars entries is the two-temperature (i.e., T-T_v) model of Park et al. [10] (referred to as Park94). That model includes collisional dissociation rate coefficients for CO_2 and CO taken from shock tube experiments carried out between 1964 and 1983. For this model, dissociation rate coefficients are described by an average temperature T_{av} which is the geometric mean of the translational temperature T and the vibrational temperature T_v. In a recent update by Johnston and Brandis [2], some of the original rate coefficient parameters from the Park94 model were adjusted to better describe CO and CO_2 emission spectra measured in the Electric Arc Shock Tube (EAST) facility at NASA Ames. In the older Mars chemistry models, little attention was given to CO_2 dissociation, because CO_2 was assumed to be rapidly dissociated for most Mars entry velocities. In these nonequilibrium chemistry models, rate coefficients for reverse reactions are obtained by microscopic reversibility ($K_{eq} = \frac{k_f}{k_r}$, with k_f and k_r defined as the forward and reverse rate coefficients, respectively, and K_{eq} is the equilibrium constant) so the flow will relax to the correct chemical equilibrium solution. Collisional dissociation of CO_2 is known to form CO and O in their ground electronic states, $^1\Sigma^+$ and ^3P, respectively. Even though CO_2 is a singlet molecule in its ground electronic state, it dissociates along a triplet potential

2

energy surface (PES). Therefore, it must undergo a transition from being on a singlet to a triplet PES. However, details about this non-radiative singlet-triplet transition are not well known.

Over the last 50 years, a number of shock tube experiments have been carried out to determine the rate coefficient for CO_2 dissociation. Early shock tube experiments were hampered by the presence of impurities, especially organic species, which greatly accelerated the dissociation process by catalytically lowering the activation energy. [11, 12] The rate coefficient used in the Park94 model was based on the shock tube experiments of Davies [13], because that was deemed the most accurate for high temperatures (even though it had an anomalously low activation energy according to [11]). Park [10] adjusted the parameter C in the Arrhenius expression ($k_D(T_{av}) = f(M) \cdot C \cdot T_{av}{}^n \cdot e^{\left(\frac{-E_D}{RT_{av}}\right)}$, where k_D is the dissociation rate coefficient, $f(M)$ is the relative efficiency of the collision partner M in promoting dissociation, E_D is the dissociation energy and R is the gas constant) to match Davies' published rate coefficient at 5000 K while keeping n fixed at 1.5 and using the accepted value for the CO_2 dissociation energy (526 kJ/mol). If the molecule were to dissociate to the lowest energy singlet asymptote, $CO(^1\Sigma^+) + O(^1D)$, E_D would be 715 kJ/mol and the exponential term in the Arrhenius expression would by 100 times smaller at $T_{av} = 5000\,K$. There have been other measurements of the CO_2 dissociation rate coefficient published since Davies' work was published. [14, 15, 16, 17] Jaffe reviewed these experiments and discussed the role of low-lying CO_2 triplet electronic states in 2011. [18] All of these experiments were carried out for dilute CO_2-noble gas mixtures, so the observed excitation and dissociation of CO_2 was due to collisions between CO_2, and Ar or Kr. For the Park94 model [10] the dissociation rate coefficients for $CO_2 + M \rightarrow CO + O$ used $f(M) = 1$ for noble gases, 15 for C, N and O atoms, and 10 for CO, CO_2, N_2, O_2 and NO molecules. When the actual data points from all of these shock tube experiments (not the Arrhenius fits) are plotted together [18], the results are seen to be in good agreement, as shown in Figure 1. The linear least-squares fit to all the data points in the figure yielded the following expression for the dissociation rate coefficient: $k_D = 3.83 \times 10^{+14} \cdot \exp(-52116/T)$ cm^3molecules^{-1}s^{-1}, where T is in Kelvin. The dissociation temperature of 52116 K corresponds to $E_D = 433.31$ kJ/mol. This rate coefficient is approximately a factor of two larger than the corresponding rate coefficient in the Park94 model.

The objective of the present study is to investigate the fundamental chemical kinetics process of CO_2 formation by recombination and determine the radiative flux from the CO_2 formed in the backshell region of spacecraft using *ab initio* quantum chemistry computations and classical mechanics simulations. This process has been studied previously at higher pressure conditions where three-body collisions stabilize the nascent product molecules. [19] However, at the low pressure conditions of interest for the present study, the frequency of three-body collisions will be much lower than the frequency of two-body collisions. Therefore, we have chosen to investigate the following recombination process:

$$CO(^1\Sigma^+) + O(^3P) \rightarrow CO_2(^3A', {}^3A'') \rightarrow CO_2(^1\Sigma^+),$$
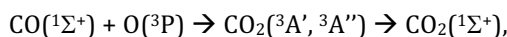
in which CO and O in their ground electronic states recombine to form triplet CO_2, followed by a transition between triplet and singlet electronic states that ultimately results in the formation of singlet CO_2. In fact, for a typical Mars entry, we estimate the mean time between collisions in the afterbody flowfield will be 0.1-0.5 μs. Actually, three triplet electronic states originate from the reactant asymptote, one of $^3A'$ symmetry and two of $^3A''$ symmetry. They are referred to as the $^3A'$, $1^3A''$ and $2^3A''$ states herein. Without a subsequent collision with another atom or molecule, the nascent triplet CO_2 will have a total energy above its dissociation limit, and will have an extremely short lifetime before it dissociates. Two-body recombination cannot occur unless there is some mechanism for triplet-to-singlet intersystem crossing. The ground state singlet potential energy surface (PES) has a seam of intersection with each of the three triplet PESs. For CO_2, each PES is a 3-dimensional hypersurface ($V(r_1, r_2, \theta)$, with r_1 and r_2 representing the two C-O bond lengths and θ the O-C-O angle), and the intersection seam has two degrees of freedom. Figure 2 shows a cut of the four PESs where the O-C-O bond angle is fixed at 110°, one C-O bond distance is fixed at 1.15 Å, which is close to r_e, the equilibrium bond length in CO_2. The other C-O bond distance is allowed to vary. The ground state curve intersects the three excited state curves at three different points. Under the Born-

Oppenheimer approximation, the triplet and singlet adiabatic PESs do not interact; thus, the triplet to singlet electronic transition is regarded as spin-forbidden. However, the true Hamiltonian contains
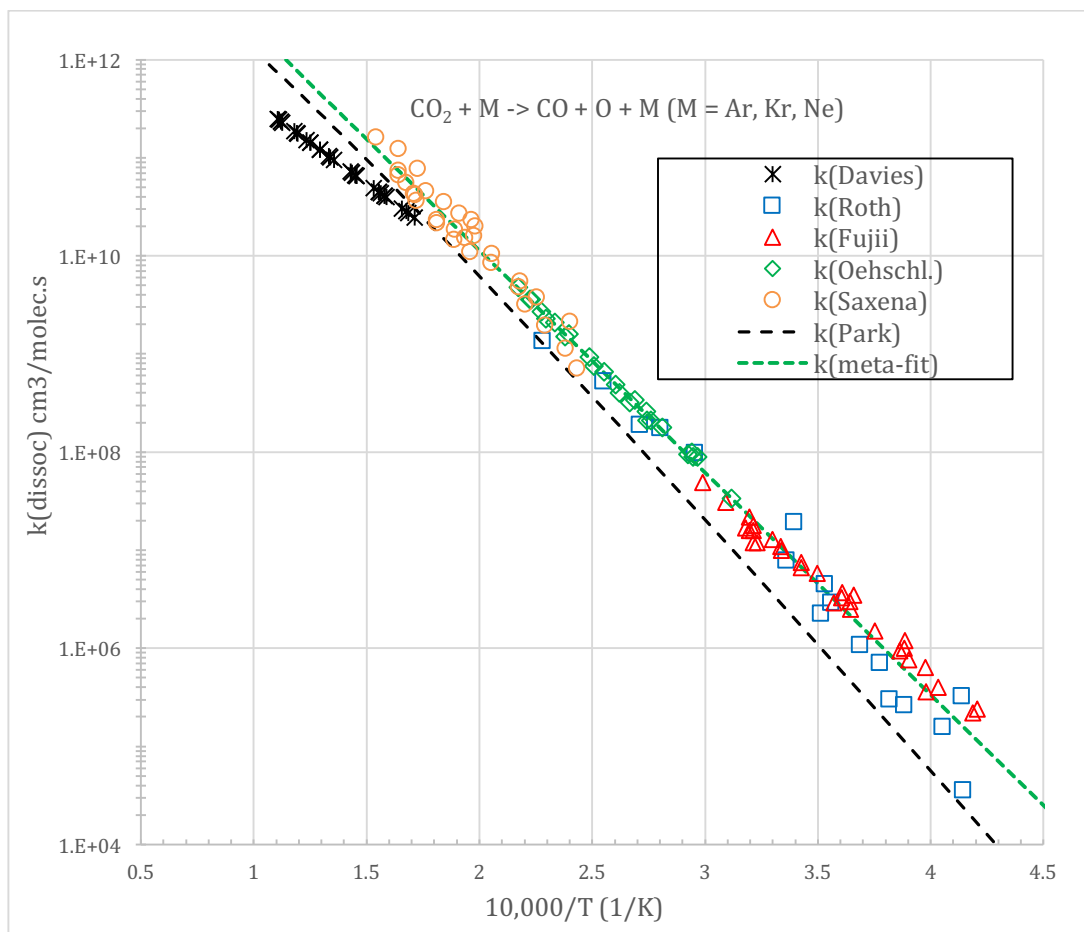
Figure 1. The measured rate coefficient data points for CO_2 dissociation from which the experimentally determined rate coefficient fits have been determined. Each color symbol represents a different experiment. The Park 94 [10] recommended rate coefficient is shown as the black dashed line. Experimental data are from Davies (stars) [13], Burmeister and Roth (blue squares) [14], Fujii (triangles) [15], Oehschlaeger et al. (diamonds) [16] and Saxena et al. (circles) [17]. The meta-fit of all the experimental data points [18] is shown as the green dashed line. Rate coefficient units are in $cm^3mol^{-1}s^{-1}$.

spin-orbit coupling terms which enable nonadiabatic electronic transitions, also known as intersystem crossing, between states of different spin multiplicities. Spin-orbit coupling [20, 21, 22, 23, 24, 25] is not only important for describing heavy elements, but it is also crucial in light atom systems. For example, it enables intersystem crossing and phosphorescence of excited triplet states in organic molecules, it alters chemical reaction paths and it leads to the fine structures in high-resolution spectroscopy. With spin-orbit coupling, there is a probability for a triplet CO_2 molecule to make a transition onto the singlet PES and become a singlet CO_2. The reverse transition is also possible, meaning there is a probability for a singlet CO_2 to transition into a triplet CO_2. The nonadiabatic transition probability is greatest when the spin-orbit coupling between the interacting states is strong. A widely-used model for describing the transition probability between two states is the Landau-Zener(LZ) model [26, 27, 28] where the transition probability is:

$$P_{LZ} = 1 - e^{\left(\frac{-2\pi H_{SO}^2}{\hbar|\partial V_3/\partial q - \partial V_1/\partial q|v}\right)},$$

where H_{SO} is the spin-orbit coupling between the singlet and triplet state, v is the nuclear velocity perpendicular to the crossing seam, and $|\partial V_3/\partial q - \partial V_1/\partial q|$ is the absolute difference between the gradients of the two PESs at the crossing point. The LZ model is based on a highly simplified description of the potential energy surfaces. Tully has developed a more general model called the "fewest switches surface hopping model" [29] that is better suited for use in classical and semiclassical scattering calculations. If the triplet-singlet transition occurs, under the conditions being considered, the nascent singlet CO_2 molecule has a ro-vibrational energy that is below its dissociation limit, $CO(^1\Sigma^+) + O(^1D)$, and thus is trapped in a high-lying ro-vibrational level of the ground electronic state. It can only relax to lower levels through subsequent collisions or photon emission.
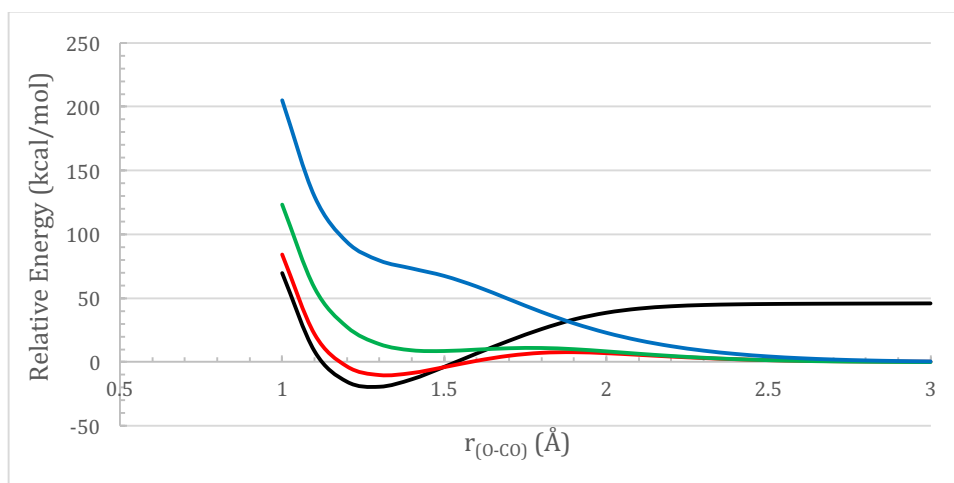

Figure 2. Calculated MRCI+Q potential energy curves of CO_2 singlet ground state and three triplet excited states as a function of OC-O distance while keeping the O-C-O bond angle θ fixed at 110º and the other C-O bond distance fixed at 1.15Å. The black curve denotes $^1A'$ state, the red curve denotes $^3A'$ state, the green curve denotes the lower $^3A''$ state and the blue curve denotes the higher $^3A''$ state. The singlet curve asymptote is $CO(^1\Sigma^+) + O(^1D)$ while the triplet curve asymptotes are $CO(^1\Sigma^+) + O(^3P)$.

The ultimate goal of the current investigation is to predict the amount of singlet CO_2 molecule formation due to the triplet-to-singlet transition, by computing the thermal rate coefficient for singlet CO_2 formation, and the distribution of CO_2 internal energy as a function of temperature and initial ro-vibrational level of CO. To achieve this goal, the first step is to compute the four PESs of CO_2 by solving the electronic Schrödinger equation using highly accurate electronic structure methods, locate the molecular geometries where the crossing between $^3A'$ and $^1A'$, $1^3A''$ and $^1A'$, and $2^3A''$ and $^1A'$ take place, obtain spin-orbit coupling matrix elements at the crossing geometries, and assess the likelihood of electronic transitions. After obtaining information on the PESs, the second step is to run surface-hopping quasi-classical trajectory calculations for $CO(^1\Sigma^+) + O(^3P)$ collisions on the four surfaces.

These calculated recombination rate coefficients can be combined with flowfields from CFD calculations to estimate the radiative heat flux on the backshell of Mars entry vehicles.

II.   Computational Methods and Results

A.   Calculated $^1A'$, $^3A'$, $1^3A''$ and $2^3A''$ potential energy surfaces and spin-orbit coupling matrix elements

The *ab initio* calculations of the electronic energy at various geometries were carried out using the Complete Active Space Self-Consistent Field (CASSCF) [30, 31, 32, 33] and Multireference Configuration Interaction (MRCI) [34, 35, 36] as formulated in the Molpro suite of quantum chemical programs. [37] In order to accurately and consistently describe the four surfaces on equal footing, all four states are included in the state-averaged full valence CASSCF and MRCI calculations combined with correlation consistent basis sets aug-cc-pVTZ [38], which properly account for electron correlation and bond breaking. This also enables us to obtain the spin-orbit coupling matrix elements between the singlet and triplet states. All calculations are performed with the Molpro Suite of quantum chemical programs (version 2010.1). [37]

We focus on regions of the PESs near the crossing seams and sampled over 9000 points. The location and energetics of the crossing points depend on the geometric variables and some of the trends we have identified based on our calculations so far are: (1) $^3A'$ crosses $^1A'$ at smaller CO-O distance compared to $1^3A''$, and much smaller compared to $2^3A''$ in general; (2) The relative energy with respect to the triplet asymptote $CO(^1\Sigma^+) + O(^3P)$ at the crossing point is lowest for $^3A'$, then $1^3A''$ and lastly $2^3A''$. This means the trajectories are most likely to have access to the crossing points of the $^3A'$ and $1^3A''$ surfaces with $^1A'$ surface. $2^3A''$-$^1A'$ crossing points lie quite a bit higher in energy compared to the other two triplet states, and the likelihood of triplet-singlet transition occurring on the $2^3A''$ surface is thus likely to be very small. In addition, the global minima on the $^3A'$ and $1^3A''$ surfaces are bound with respect to the triplet asymptote while global minimum on the $2^3A''$ surface is not. thus we are going to focus on the $^3A'$ and $1^3A''$ surfaces; (3) As the bond angle θ increases, the $^3A'$-$^1A'$ crossing points increase in energy, and the $^3A'$-$^1A'$ and $1^3A''$-$^1A'$ crossing points become closer together. Figure 2 and Figure 3 are two example cuts of the four PESs with the bond angle θ fixed at 110° and 140°, respectively. As expected, the $^1A'$ curve has a much deeper well. Earlier lower-level *ab initio* calculations by Hwang and Mabel [39] reported similar crossing geometries for the lowest-energy singlet and triplet electronic states of CO_2.
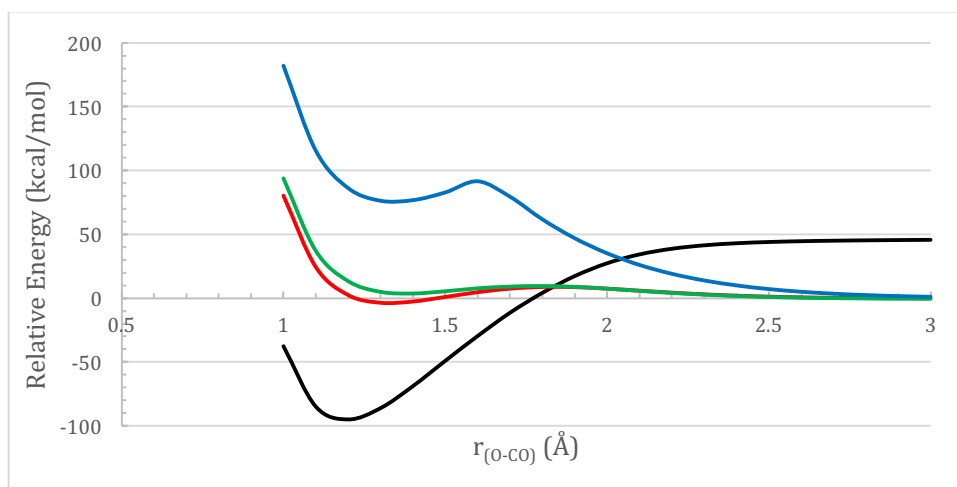

Figure 3. Calculated MRCI+Q potential energy curves of CO_2 singlet ground state and three triplet excited states as a function of OC-O distance while keeping the O-C-O bond angle θ fixed at 140° and the other C-O bond distance fixed at 1.15Å. The black curve denotes $^1A'$ state, the red curve denotes $^3A'$ state, the green curve denotes the lower $^3A''$ state and the blue curve denotes the higher $^3A''$ state. The singlet curve asymptote is $CO(^1\Sigma^+) + O(^1D)$ while the triplet curves asymptote is $CO(^1\Sigma^+) + O(^3P)$.

The spin-orbit coupling matrix elements are computed using the full Breit-Pauli operator implemented in Molpro [40] with the adiabatic MRCI wavefunctions. There are three Cartesian components of the spin-orbit Hamiltonian, LS_X, LS_Y and LS_Z. For $^3A'$-$^1A'$ coupling, only the LS_Z component is non-zero, while for $^3A''$-$^1A'$ and $^3A'$-$^3A''$ coupling, both the LS_X and LS_Y components are non-zero. The transition probability depends on the strength of the spin-orbit coupling, and the coupling matrix elements depend on the geometric variables. Figures 4 and 5 show the spin-orbit coupling matrix elements as a function of CO-O distance while keeping the angle θ fixed at 110° and 140 °, respectively, with the other C-O bond distance kept fixed at 1.15 Å, corresponding to Figures 2
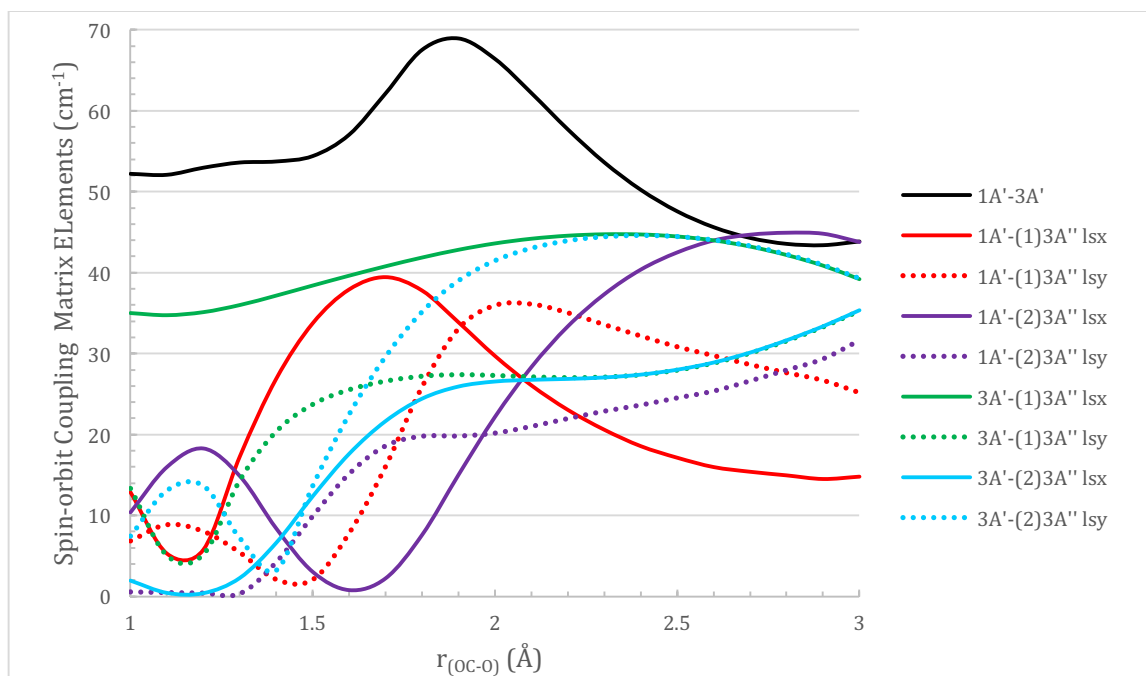

Figure 4. Spin-orbit coupling matrix elements as a function of OC-O distance while keeping the angle θ fixed at 110° and the other C-O bond distance at 1.15 Å (the same geometries as in Figure 2). The black curve denotes the $^3A'$-$^1A'$ spin-orbit coupling matrix element LS_Z, the red solid curve denotes the $1^3A''$-$^1A'$ coupling matrix element LS_X, the red dashed curve denotes the $1^3A''$-$^1A'$ coupling matrix element LS_Y, the purple solid and dashed curve denote the $2^3A''$-$^1A'$ coupling matrix element LS_X and LS_Y, respectively, the green solid and dashed curve denote the $1^3A''$-$^3A'$ coupling matrix element LS_X and LS_Y, respectively, and the blue solid and dashed curve denote the $2^3A''$-$^3A'$ coupling matrix element LS_X and LS_Y, respectively.

and 3. The coupling matrix elements vary with the OC-O distance and $^3A'$ has the strongest coupling with $^1A'$ overall. We have focused on evaluating the matrix elements for geometries near the crossing seams since what matters the most are the spin-orbit coupling strengths in those regions. Figure 6, 7, and 8 plots the matrix elements as a function of the energy difference between the coupling states. A small energy range, ±1 kcal/mol, is chosen for the plots. For $^3A'$-$^1A'$, the coupling matrix elements are in between 50 and 85 cm^{-1}. For $1^3A''$-$^1A'$, the LS_X component mostly lies between 30 and 40 cm^{-1} while the LS_Y component lies in between 0 to 40 cm^{-1}. The $2^3A''$ and $^1A'$ surface cross at about ten calculated points, because we are focusing on the crossing between the lower-lying triplet surfaces
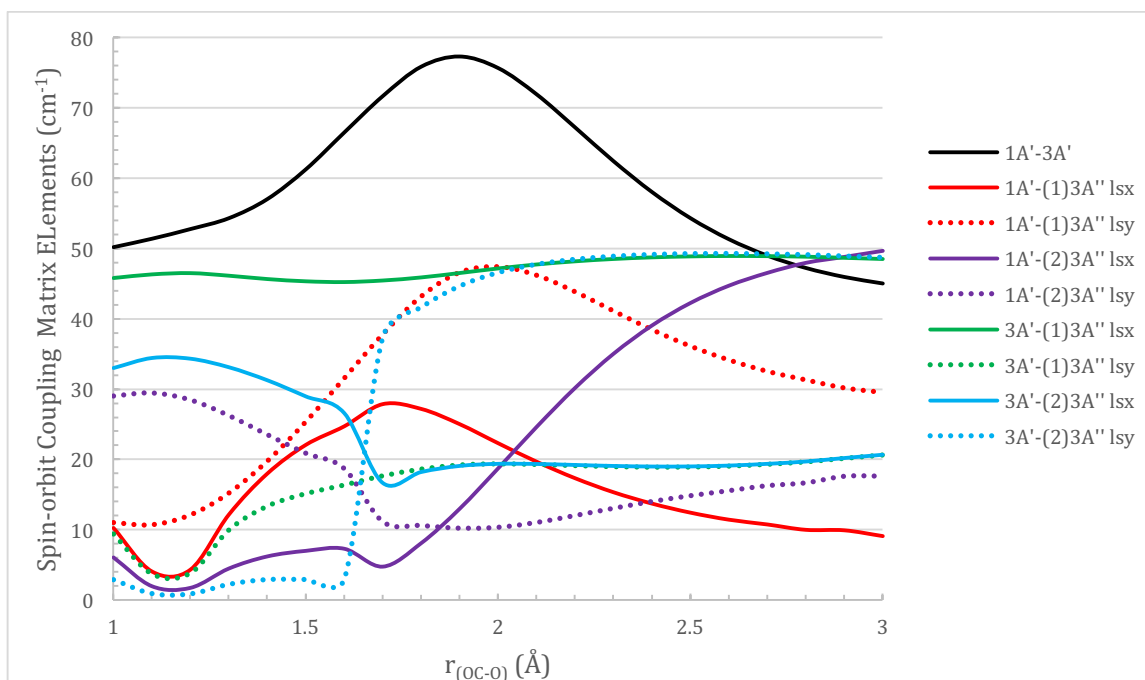
Figure 5. Spin-orbit coupling matrix elements as a function of OC-O distance while keeping the angle θ fixed at 140° and the other C-O bond distance at 1.15 Å (the same geometries as in Figure 3). The black curve denotes the $^3A'$-$^1A'$ spin-orbit coupling matrix element LS_Z, the red solid curve denotes the $1^3A''$-$^1A'$ coupling matrix element LS_X, the red dashed curve denotes the $1^3A''$-$^1A'$ coupling matrix element LS_Y, the purple solid and dashed curve denote the $2^3A''$-$^1A'$ coupling matrix element LS_X and LS_Y, respectively, the green solid and dashed curve denote the $1^3A''$-$^3A'$ coupling matrix element LS_X and LS_Y, respectively, and the blue solid and dashed curve denote the $2^3A''$-$^3A'$ coupling matrix element LS_X and LS_Y, respectively.

with the singlet surface, and both the LS_X and LS_Y matrix elements are between 0 and 30 cm^{-1}. Hwang and Mebel [39] computed values for the spin-orbit coupling matrix element of 20.3 cm^{-1} for the lowest energy singlet-triplet crossing geometry in C_{2v} symmetry (OCO bond angle of 105° and CO bond lengths of 1.26 Å) and 89.5 cm^{-1} for a linear geometry with CO bond lengths of 1.13 and 1.90 Å.

B. Analytical representations of $^1A'$, $^3A'$, $1^3A''$ and $2^3A''$ potential energy surfaces

In order to run trajectories, we need good analytic representations for the four surfaces. For the three triplet surfaces, we use the surfaces from our previous work. [41] While those triplet surfaces did not include the present data in their determination and the emphasis was on other regions of the PES rather than the singlet-triplet crossing seams, they provide a useful base to start this study. The predicted shape of the PES in the vicinity of the crossing seams is in good agreement with the present calculations, although the overall energy is shifted somewhat. In our dynamics calculations, we shift the triplet PES in energy to best match the closest crossings from the present *ab initio* calculations. We will say more about this shift after the discussion of the singlet PES.

For the singlet surface, we constructed an analytic representation that included both the *ab initio* results from the MRCI calculations described above and *ab initio* results from Ref. [42], that emphasized the global minimum of the ground electronic state of CO_2. To facilitate the determination of this new analytical representation, we needed to have as similar quality data from the two sets of *ab initio* calculations. Thus, we computed MRCI energies at 15 geometries near the CO_2 minimum that were included in the Huang et al. data set. From Ref. [42] we used the ACPF data computed using the triple zeta basis. We compared these results at the 15 common geometries with our MRCI results as
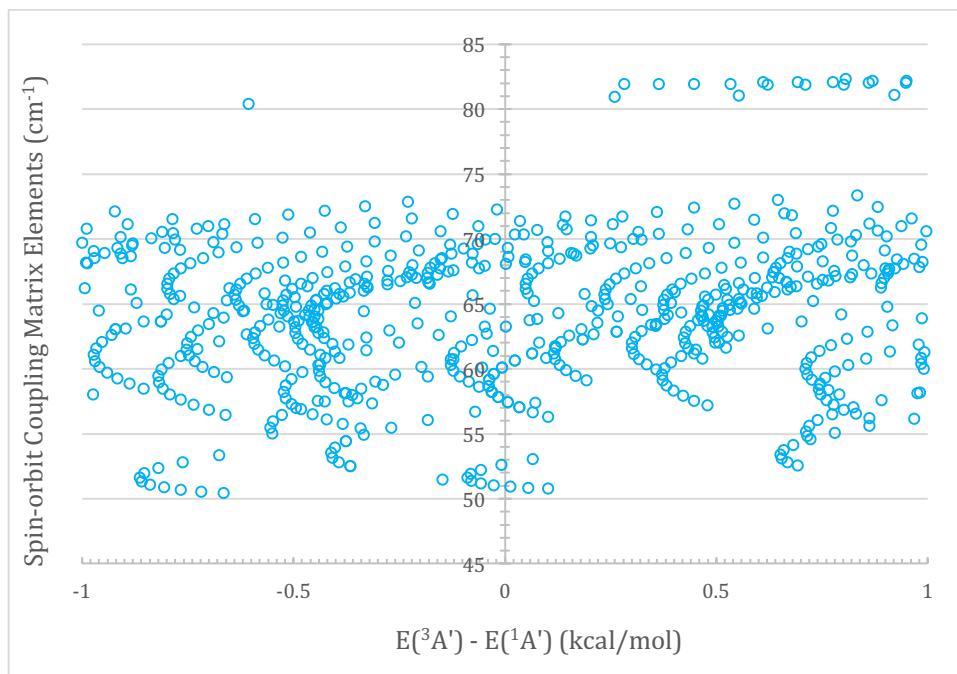
8

Figure 6. Scattered plot of $^3A'$-$^1A'$ spin-orbit coupling matrix element LS$_Z$ as a function of the energy difference between the $^3A'$ and $^1A'$ state near the crossing seam, within ±1 kcal/mol difference in energy.
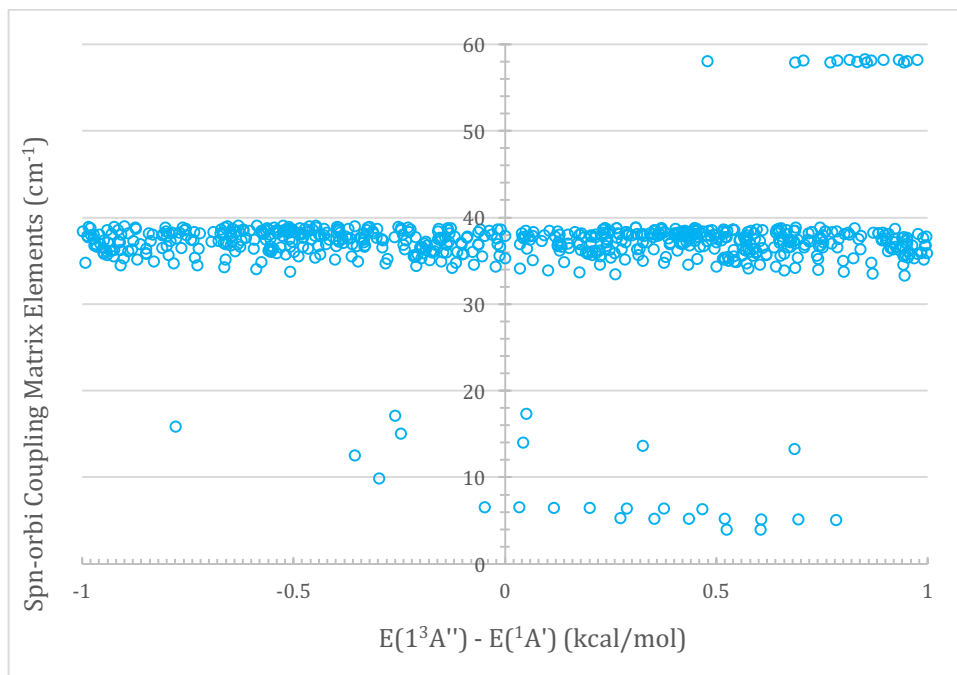

Figure 7. Scattered plot of $1^3A''$-$^1A'$ spin-orbit coupling matrix element LS$_X$ as a function of the energy difference between the $1^3A''$ and $^1A'$ state near the crossing seam, within ±1 kcal/mol difference in energy.
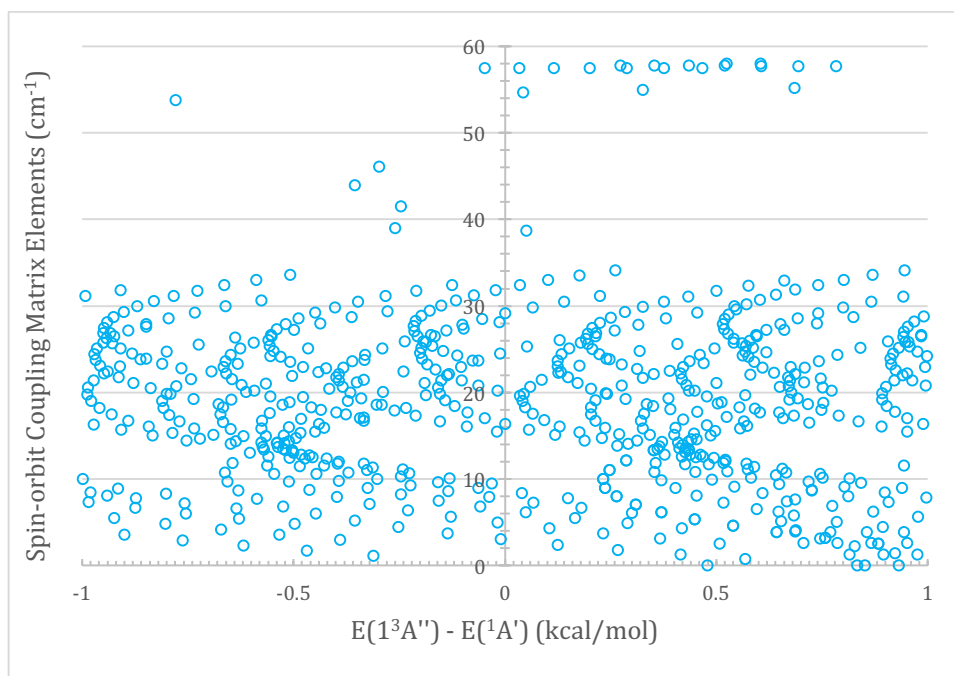
9

Figure 8. Scattered plot of $1^3A''$-$^1A'$ spin-orbit coupling matrix element LS_Y as a function of the energy difference between the $1^3A''$ and $^1A'$ state near the crossing seam, within ±1 kcal/mol difference in energy.

well as our MRCI+Q results. We found that the root-mean-square (rms) deviation from the average difference to be significantly smaller for the MRCI+Q results, so we used them in the new analytic representation. The rms deviation from the average difference was 0.47 mE_h (approximately 1 kJ/mol). For this analytic representation, we used the same functional form as for the triplet surfaces, with the exception that in the CO+O asymptote, the CO potential curve was taken to be the minimum of $CO(^1\Sigma^+) + O(^1D)$ and $CO(^3\Pi) + O(^3P)$. The $CO(^3\Pi)$ potential curve was taken from extensive icMRCI calculations using the cc-pVTZ basis with two sets of diffuse functions on C and three on O. [43] The non-bonding interaction parameters for CO+O and $C+O_2$ diabats [41] were fixed at the values found for the $^3A'$ surface, but the modulating/damping function was set to unity. In the bound CO_2 diabat, an eighth order expansion was used. Since the available singlet *ab initio* data did not cover the full range of coordinate space, we had some difficulty ensuring that the final analytic representation behaved physically for all geometries of interest yet also gave a satisfactory representation of the *ab initio* data. In the end, we performed a fit with only a fourth order expansion, and this was used to generate a set of constraint data points to ensure that nothing untoward happened when using the eighth order fit. In the final fit, 8849 icMRCI+Q points, 577 icACPF points, and 55,000 constraint points were included. The icMRCI+Q points had uniform weight equal to 577/8849, the constraint points had uniform weight 5.77/55000, and the weight for the icACPF point i was $1/\max(0.01E_h, E_i - E_{min})$, where E_{min} is the energy at the CO_2 singlet minimum. As before [41] we checked the percentiles of the fitting errors and removed points that seemed to be outliers. We removed 49 icMRCI+Q energies and 31 icACPF energies.

Because of the unequal weights in the least squares fit, it is hard to characterize the quality of the fit with a single number. Instead we plot some comparisons. In Figure 9, we plot the fitted energy vs. the calculated energy. A perfect fit would lead to points all lying on the line x=y. The zero of energy for the plot is the global minimum of the potential. We see small differences between fitted and calculated energies over the entire range. For reference, the computed dissociation energy to $CO(^1\Sigma^+) + O(^1D)$ is 255 mE_h (675 kJ/mol). Next, in Figure 10 we show the quality of the fit close to the minimum. The low lying ACPF energies are fit to within ±0.2 mE_h while the low lying MRCI+Q energies are fit to within about ±0.5 mE_h. The difference in quality of the fits is perfectly consistent

10

with the 0.47 mE$_h$ rms deviation between the two sets of *ab initio* calculations at the common set of geometries. The Harmonic vibration frequencies computed from this surface are ω_{SS}=1348 cm^{-1}, ω_B=665 cm^{-1}, and ω_{AS}=2362 cm^{-1}, where SS is the symmetric stretch, B is bend, and AS is antisymmetric stretch. In comparison, the values from the very accurate PES of Ref.[42] are 1354, 673, and 2396, respectively. Thus, this is a very satisfactory fit.

We have to set a reference energy (i.e., a zero of energy) for some CO_2 geometry that is accurately represented on all the PESs. Ideally, the zero of energy for the triplet and singlet PESs is determined from their separated atom limits, using the experimentally determined $O(^1D)$ - $O(^3P)$ energy difference. However, this region is not sampled in the *ab initio* data used for the singlet PES determination, so this is not a useful method. Alternatively, we could set the zero of energy by making the $CO(^1\Sigma^+)$ + $O(^1D)$ energy relative to the $CO(^1\Sigma^+)$ + $O(^3P)$ equal to the experimental value [44] of 15,870 cm^{-1}. But, as mentioned above, while the analytic representations of the triplet PES reproduce well the shape in the vicinity of the crossing seams, there are systematic differences away from the crossing seams. We compared the triplet analytical representation to the calculated triplet energies at all geometries where the computed difference between the singlet and triplet energies was less than 0.1 mE$_h$ and we computed the average difference and rms deviation from the average. For the $^3A'$ PES, the average difference and rms deviation for 42 energies was 173.6 and 6.4 mE$_h$ respectively and for the $1^3A''$ surface, the average difference and rms deviation for 22 energies was 158.1 and 7.9 mE$_h$ respectively. There is only one crossing energy satisfying this criterion for the $2^3A''$ surface: the difference there is 157.6 mE$_h$. Because of the 15 mE$_h$ difference in shift, it doesn't make sense to couple more than one triplet PES in the dynamics calculations. We will eliminate this difficulty in future work by refitting the triplet potentials including the present *ab initio* results along with the original *ab initio* results used to determine the analytical representation. [41] With this zero of energy for the $^3A'$ PES, the difference in energy between $CO(^1\Sigma^+)$ + $O(^1D)$ and $CO(^1\Sigma^+)$ + $O(^3P)$ is 58.6 mE$_h$ (12,861 cm^{-1}), i.e. 81% of the experimental value.

The geometry with the lowest singlet energy, where we compute a crossing, occurs at a CO bond length of 1.190 Å. This is quite close to the global singlet CO_2 minimum with a CO bond distance of 1.17 Å. In Figure 11 we show a contour plot of the singlet PES for one CO bond length fixed at 1.17 Å. We also show the geometries of the *ab initio* calculations for one CO bond length being within 0.03 Å of 1.2 Å. The deep well is clearly seen and there is a barrier to dissociation of about 16 mE$_h$. We also show the crossing seam ± 20 mE$_h$. In Figure 12 we show the same set of contours for the $^3A'$ PES. Although there is an attractive region for the $^3A'$ PES [41], the main reason for the attractive contours is because the zero of energy is the same as for the singlet PES, namely the $CO(^1\Sigma^+)$ + $O(^1D)$ energy of 58.6 mE$_h$.

C.   Surface hopping quasi-classical trajectory dynamics

The surface hopping calculations were carried out using a modification of the trajectory code described previously. [45] This is a vectorized variable stepsize trajectory code (VVTC) that has been used for many different collision processes. We implemented the fewest switches algorithm of Tully [29] with the additional decoherence correction of Granucci and Persico. [46] This is done by adding 2N^{surf} additional coupled equations to the equations of motion for the trajectory, where N^{surf} is the number of surfaces coupled. These additional equations govern the time dependence of the real and imaginary parts of the amplitude on each surface. Once the zero of potential energy was shifted to be at the $CO(^1\Sigma^+)$ + $O(^3P)$ minimum, we had no trouble accurately integrating these additional equations. This shift was required because although the trajectories themselves do not depend on the zero of energy but rather just on the gradient of the energy, the leading contribution to the phase of the amplitude is proportional to the current potential energy times time. In our initial calculations, the zero of energy was taken to be the fully dissociated separated atom limit, and since the energy of $CO(^1\Sigma^+)$ + $O(^3P)$ minimum is about -190 E$_h$ with respect to that zero, we obtained extremely rapid phase changes that were hard to track accurately.

Our code automatically cuts down the time step when the amplitudes change rapidly, so we have no trouble identifying regions where hopping can occur. It is convenient for debugging purposes to make trajectories independent of whether they are run individually or in a vectorized group. In the unmodified code, this is done by setting up the initial conditions sequentially, so the random number string is the same in both cases. The addition of hopping introduces the need for random numbers along the trajectory, so the previous strategy is no longer effective. The way we solved this problem was to use a different random number generator for hopping than was used to set up the initial conditions. Since the hopping random numbers are only used sequentially, the random number generator does not need to be as sophisticated as we use for the initial conditions. [45] Thus we used the routine ran0 from Press et al. [47] with the initial seed generated from the random number generator used to generate the initial conditions.
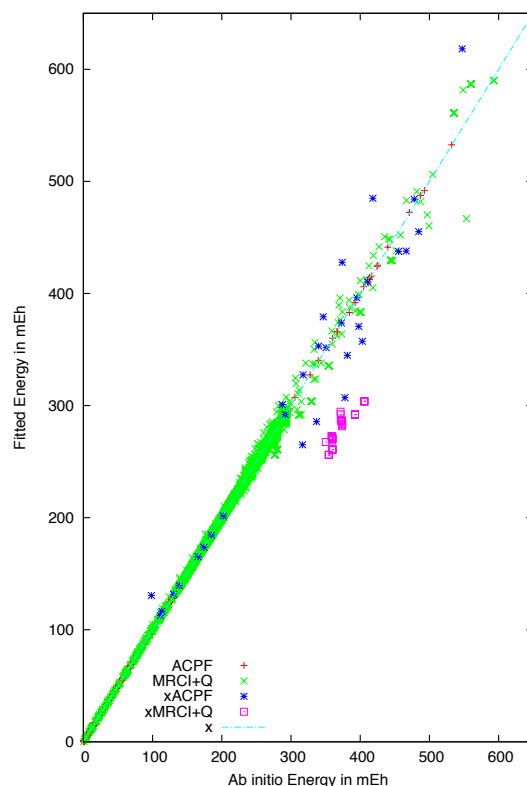

Figure 9. Fitted singlet energies vs. *ab initio* energies. The red + are the ACPF energies, green x are the icMRCI energies, blue stars are discarded ACPF energies, and pink squares are discarded MRCI+Q energies.
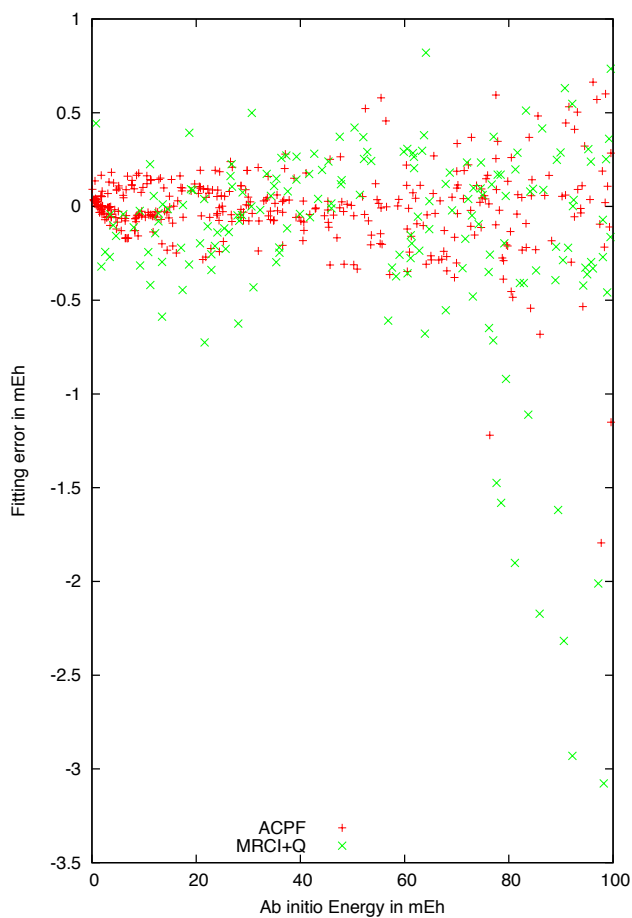
Figure 10. Fitting errors near the minimum of the singlet PES. The red + are the ACPF energies and the green x are the icMRCI energies.
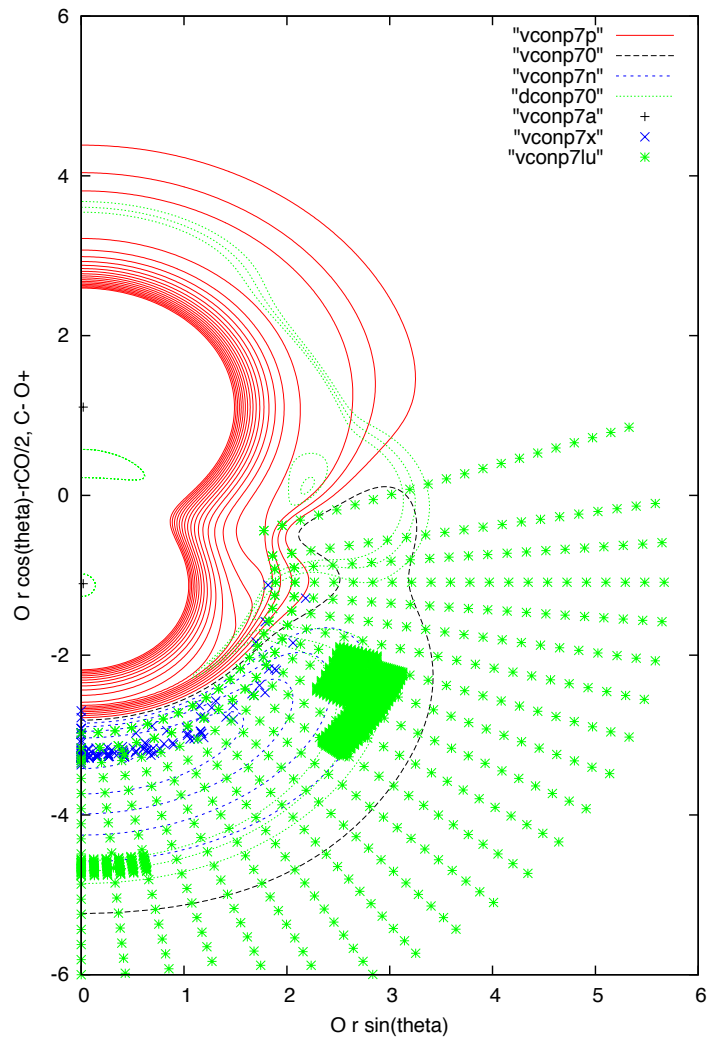
Figure 11. The singlet PES with one CO bond length fixed at 2.201 bohr (1.165 Å). One O atom is on the y axis at 1.1005 and the C atom is on the y axis at -1.1005. The contours show the energy when the other O atom is at that position. The zero of energy is CO($^1\Sigma^+$) + O(^{1}D), and the gray contour line is for this energy. The blue (red) contour lines show negative (positive) energies in steps of 50mE$_h$. The green contour lines show the crossing seam ±20mE$_h$. The blue symbols mark the ACPF energy geometries, and the green symbols the MRCI+Q geometries.
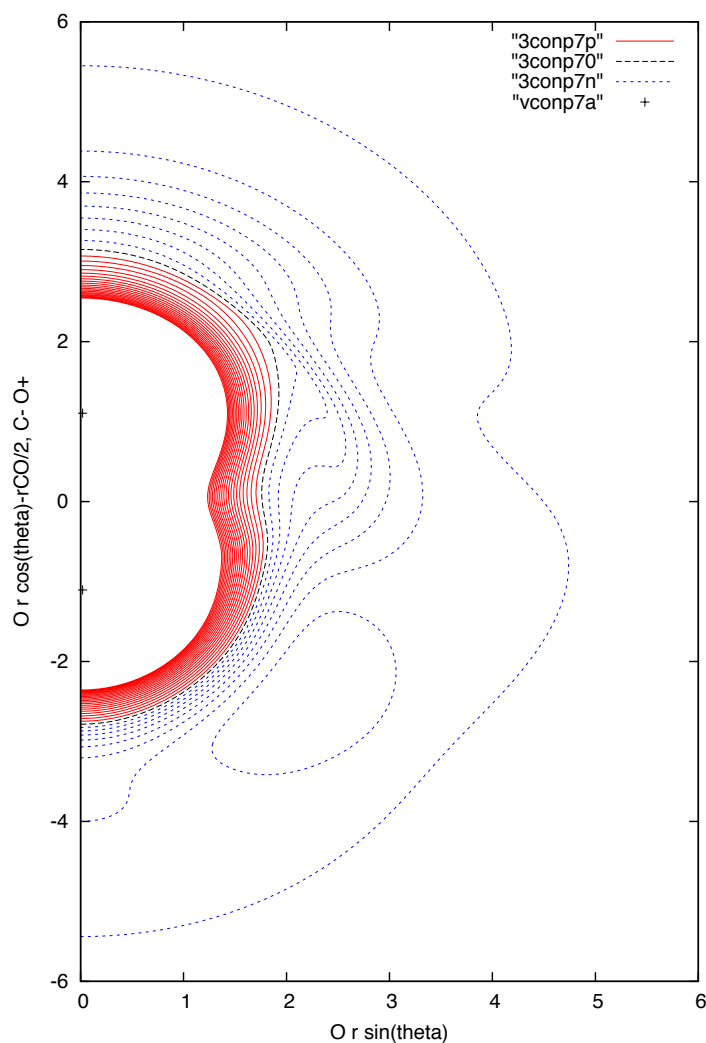
14

Figure 12. PES for ^{3}A' at the same fixed CO bond length as in Figure 11.

We carried out trajectories using both the adiabatic electronic basis and the diabatic electronic basis. In the adiabatic electronic basis, we diagonalize the electronic Hamilton in the diabatic basis whenever the potential energy or its gradients are required. In this case, the coupling is determined by the matrix element $\langle K|d/dQ_i|N\rangle$, where K labels the current electronic state and N labels a generic electronic state, and Q_i is one of the coordinates being following along the trajectory. This quantity is given by $\langle K|d/dQ_i|N\rangle = -\sum_{nm} V_{nk}\frac{dH_{nm}}{dQ_i}V_{mN}/(E_K - E_N)$, where n and m label diabatic states, V_{nK} is the eigenvector for adiabatic state K, H_{nm} is the diabatic electronic Hamiltonian, and E_K is the adiabatic energy for adiabatic state K. This coupling is quite small except in the vicinity of crossing seams, where it can become quite large. Thus, trajectories encountering a crossing seam have a very high probability of hopping even if the diabatic coupling is small and the physical effect is to follow the diabatic surface. In this case, the surface hopping algorithm corrects this sudden hop by hopping back down usually in less than a picosecond. This result, however, is not consistent with the philosophy of the fewest switches algorithm. In contrast, if the trajectory is carried out in the diabatic basis, the coupling is solely determined by H_{nm}, which is taken to be a constant, because the magnitude of spin orbit coupling is nearly constant over the range of geometries considered. Based on our calculations of the spin orbit matrix elements, we used a value

15

of 100 cm^{-1} for the present calculations. Thus, the frequency of hopping is much lower than in the adiabatic basis but, as the coupling never goes to zero, the electronic state amplitudes show small amplitude oscillation even when the collision partners are widely separated. Also, when we correct the kinetic energy after a hop [29], we base this correction on $\langle K|d/dQ_i|N\rangle$ even though we follow the trajectories in the diabatic basis. Neither the adiabatic or diabatic basis is obviously superior to the other, and we choose the diabatic basis for all our calculations reported here. Furthermore, because of the reference energy issues described above, we only couple the singlet PES to the ^{3}A' surface.

We carried out two kinds of calculations: one starting with $CO(^1\Sigma^+)$ + $O(^3P)$, and one starting with singlet CO_2. In the former case, we sampled CO ro-vibrational levels from a Boltzmann distribution at 5000K and initial relative translational energies of 10, 15, 20, 25, 30, 35, 40, 45, 50, 55, and 60 mE$_h$ (26.25 to 157.5 kJ/mol). We ran 120,000 trajectories for each initial relative translational energy, and integrated each trajectory until either an atom plus a diatom emerged from the collision or the time of the trajectory exceeded 10^6 atomic units of time. This time limit is about 24 picoseconds. For all collision energies, there were some trajectories that were stopped at this 24 picosecond limit, but only a handful. Results for a typical initial condition (E_{REL} = 30 mE$_h$) are shown in figure 13, where we plot the number of hops vs. the time delay. The time delay is computed as the time of the trajectory minus the time the O would need to reach the center of mass of the CO from the
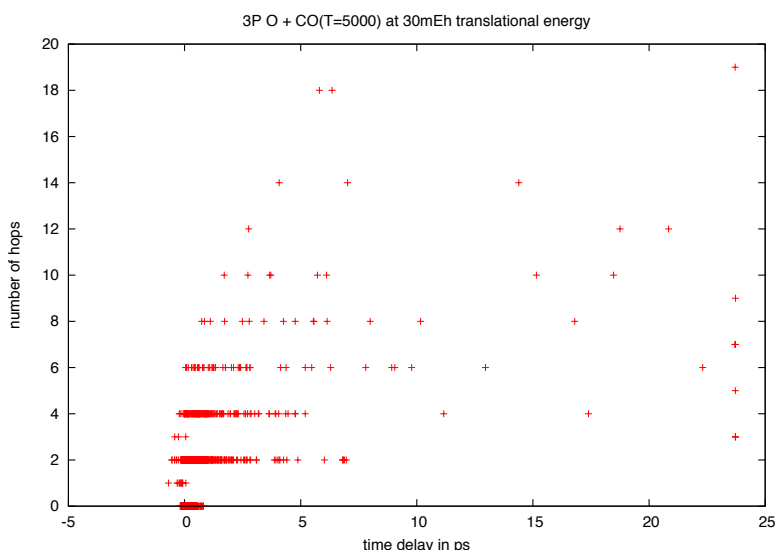

Figure 13. Number of hops vs. time delay for O(^{3}P) + CO($^1\Sigma^+$) at a relative translational energy 30 mE$_h$ (78.8 kJ/mol).

start of the trajectory in the absence of interatomic forces minus the time the O would require to leave the center of mass of the CO to the end of the trajectory in the absence of interatomic forces. Due to the repulsive nature of the interaction when O gets close to CO, some time delays are negative. For this E_{Rel}, most trajectories led to an unstable singlet CO_2 molecule that fell part within about 12 picoseconds, but 6 were still bound after 24 picoseconds. Thus, the probability of forming a long-lived singlet CO_2 molecule is on the order or 10^{-4}. This results in poor statistics for elucidating the lifetimes, thus we carried out the second type of calculations that can be construed as a way to directly focus on only the trajectories that formed $^1CO_2$ with any appreciable lifetime. In this approach, we study the reverse process, dissociation of energetic CO_2 molecules by hopping to the lowest-energy triplet PES.

The specification of the initial conditions for a diatomic molecule are well known, but the specification of the initial conditions for a triatomic has posed significant difficulties. The problem

16

relates to the fact that for a diatomic, the vibrational motion is decoupled from the rotational motion, only depending on the rotational angular momentum, while the rotational motion is simply driven by the vibrational motion. [48] In contrast for a triatomic, all vibrations and rotations are fully coupled. The customary generalization to triatomics is the determination of good action-angle variables that describe the motion of the triatomic in terms of separable motions, however this is not possible to do systematically, for the coupled motion can lead to resonances or chaotic trajectories that so distort phase space that the determination of good action-angle variables becomes impossible. In our study of the H_2O molecule [49], we found that only a few vibrational levels could be determined when adding rotation, because chaotic trajectories were found with only small amount of rotational angular momentum.

Thus, in the present work we use a different tactic. We will only specify an initial energy for a metastable CO_2 molecule (one with total energy higher than the lowest $CO(^1\Sigma^+) + O(^3P)$ asymptote and lower than the $CO(^1\Sigma^+) + O(^1D)$ asymptote), and randomly sample over all possible vibrational and rotational motion. We do this by specifying the Cartesian Radau [50] vectors describing the CO_2 molecule in a laboratory fixed frame of reference and use uniform sampling for each component of the vectors within the interval ±1.3 Å. We evaluate the potential energy at this geometry and if this energy is greater than the target energy, we sample again and repeat until an energy less than the desired energy was obtained. When position coordinates are obtained that satisfy the constraints, we use uniform sampling to obtain the time derivatives of all but one coordinate. The sampling box size was set to the maximum allowable time derivative based on the available kinetic energy. The remaining time derivative was computed from the square root of the difference between the available kinetic energy and the kinetic energy from the other components. If this difference was negative, another trial was made until the difference was positive. Then finally we randomly chose the sign of the square root term.

For these calculations, we ran a batch of 100 trajectories for each of the energies used for the recombination calculations. We analyzed the results by looking at the times for dissociation, computed like the time delay described above. This analysis is only valid if each trajectory is equally weighted, which is what we have done in the present work. More careful consideration of the initial conditions shows unequal weights will be required but that is beyond the scope of the present work. We sort the trajectories in order of the dissociation time, and a typical result is shown in Figure 14 where we show the results for an initial energy of $30mE_h$, the same as used for Figure 13. We show results for two different maximum integration times: 48 picoseconds and 480 picoseconds. Note that the latter integration time is ~1000 times shorter than the mean time between collisions in the afterbody flowfield. In both cases, we find trajectories that never dissociated, and of the trajectories that did dissociate, we can fit the dissociation percent reasonably well with a half-life of 6 picoseconds. In this fit, we scaled the lifetime plot so 100% fell at 76%, i.e. 24% of the trajectories were assumed unable to dissociate for this analysis. These results seem to be consistent with those shown in Figure 13.

It is not yet clear why 24% of the trajectories were unable to dissociate. There are a few different possibilities, but it seems likely that there are at least two different regions of phase-space, 76% falling into one region and 24% falling into the other, and there is some barrier between them. Whether this is a barrier that would manifest itself in accurate quantum calculations, or some sort of artifact of classical mechanics, remains a question for further research. Nonetheless, in Table 1 we give the half-lives and percentage of dissociation determined from the present work.
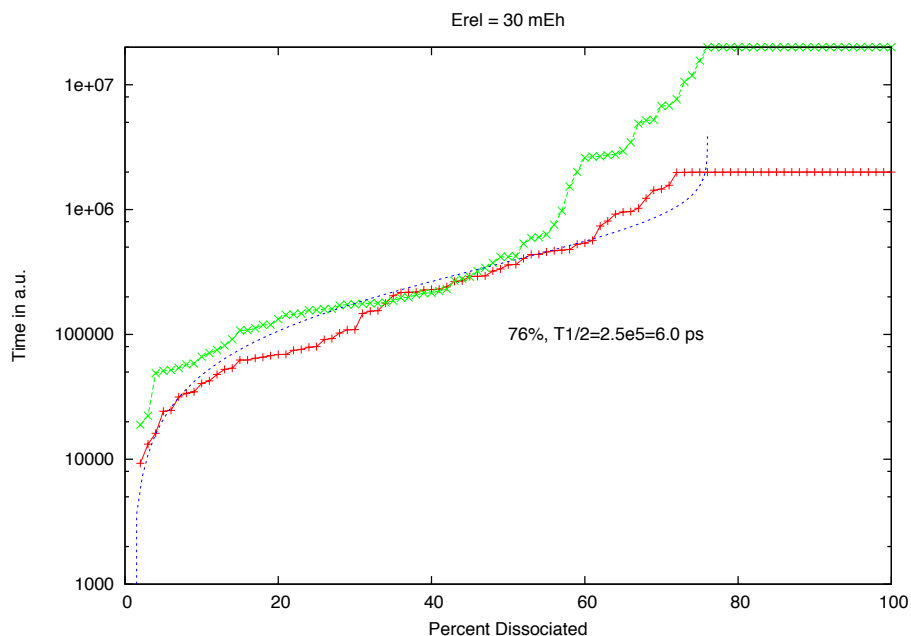
Figure 14. The dissociation time as a function of percent dissociated for the same energy as Figure 13. The results are given for two different maximum integration times (48 ps in red and 480 ps in green) are given, along with the fitted decay function (dotted line).

The recombination rate for $CO(^1\Sigma^+)$ + $O(^3P)$ to form singlet CO_2, was then estimated. To properly compute this rate, we need to solve the master equation, and this involves following the populations of the various states of CO_2 as a function of time, which requires state-to-state rate coefficients – this is beyond the scope of the present work. Nonetheless we can make some reasonable simplifying approximations: see Refs. [45] and [51] where a comparison is made between accurate calculations and the simplified calculations described below. The results were within a factor of about 2. To compute the rate coefficient for CO + O + M $\rightarrow CO_2$ + M, we assume the three-body recombination for the process takes place by a two-step mechanism: CO + O $\Leftrightarrow CO_2^*(i)$, followed by $CO_2^*(i)$ + M $\rightarrow CO_2$ + M. In these reactions, i represents a metastable state, i.e. one with energy between the triplet and singlet asymptotes. We approximate all metastable states by the levels with the energies for which we have computed lifetimes – see Table I. These computed lifetimes satisfy the equilibrium criterion in Ref. [45]. Assuming the first step of this mechanism is in equilibrium, the three-body recombination rate is given by $k^{3B} = \sum_{in} K_{eq}^i(T) k_{in}^f(T)$, where K_{eq}^i is the equilibrium constant, and k^f is the de-excitation rate. The sum over *i* includes all CO_2 lying between the triplet and singlet dissociation limits, and the sum over *n* includes all bound states of CO_2. We use, as a rough estimate, the value of 28 Å^2 for the cross section for the de-excitation process summed over *n*. This makes $k_{in}^f(T)$ equal to 10 times the average velocity. The equilibrium coefficient is given by the ratio of the partition functions for CO+O and $CO_2^*(i)$. The atomic and CO partition functions are easily computed, the CO_2 partition function is much more complicated. To compute it we need to know the density of the $CO_2^*(i)$ states as well as the total density of states for the CO_2 molecule. We will estimate this via a procedure similar to that used to generate the initial conditions of the trajectories starting as singlet CO_2. This calculation is currently in progress.

Given the low probability for CO_2 recombination (10^{-4}) coupled with the rather low collision frequency predicted for the afterbody flowfield, it seems unlikely that a significant amount of singlet CO_2 can be formed by this mechanism. Therefore, other processes should be considered, such as the exchange reaction CO + $O_2 \Leftrightarrow CO_2$ + O and stabilization of metastable $CO_2^*(i)$ by photoemission.

18

Table 1. Summary of Classical Trajectory Results for Metastable CO_2

Total energy of CO_2 in $mE_h{}^a$	Half Life in ps	% that dissociated
20	13	63
25	18	63
30	6.0	76
35	4.8	77
40	2.9	81
45	2.4	85
50	2.4	90
55	2.4	90
60	1.5	94

    a   Energy relative to $CO(^1\Sigma^+) + O(^3P)$

III. Summary

In this work, we have focused on the two-body recombination reaction of CO_2, in which a ground electronic state CO molecule and a triplet state oxygen atom collide and make a transition to the singlet potential energy surface of CO_2. We computed the four relevant potential energy surfaces (one singlet and three triplet) and the spin-orbit coupling elements between them for CO_2 using *ab initio* quantum chemistry methods. We used the calculated PES data to obtain and calibrate analytical expressions for these potentials and we used them for surface hopping classical trajectory calculations based on Tully's fewest switches surface hopping algorithm. The results of the trajectory calculations indicate that the probability of a triplet-to-singlet transition is approximately 10^{-4}. Calculation of the recombination rate coefficients, for temperatures characteristic of the afterbody flowfields of Mars entry vehicles, are in progress. It is unlikely that this recombination reaction is responsible for the larger than expected afterbody heating that has been measured during the Mars Science laboratory entry. We are also computing CO_2 dissociation rate coefficients (the reverse process of recombination) using the same surface hopping method. This work represents the first theoretical study of these reactions for CO_2 that incorporates an accurate treatment of the singlet-triplet transition.

Acknowledgement

References

[1] P. R. Mahaffy, C. R. Webster, S. K. Atreya, H. Franz, M. Wong, P. G. Conrad, D. Harpold, J. J. Jones, L. A. Leshin, H. Manning, T. Owen, R. O. Pepin, S. Squyres, M. Trainer and MSL Science Team, "Abundance and Isotopic Composition of Gases in the Martian Atmosphere from the Curiosity Rover," *Science,* vol. 341, pp. 263-266, 2013.

[2] C. O. Johnston and A. M. Brandis, "Modeling of Nonequilibrium CO Fourth-Positive and CN Violet Emission in CO_2-N_2 Gases," *J. Quant. Spect. Rad. Transfer,* vol. 149, pp. 303-317, 2014.

[3] S. A. Tashkun and V. I. Perevalov , "CDSD-4000: High-Resolution, High-Temperature Carbon Dioxide Spectroscopic Databank," *J. Quant. Spect. Rad. Transfer,* vol. 112, no. 9, pp. 1403-1410, 2011.

[4] M. L. da Silva and J. Beck, "Contribution of CO_2 IR Radiation to Martian Entry Radiative Wall Fluxes," in *AIAA2011-0135*, Orlando, 2011.

[5] K. Fujita, S. Matsuyama and T. Suzuki, "Prediction of Forebody and Afterbody Heat Transfer Rate for Mars Aerocapture Demonstrator," in *AIAA2012-3001*, New Orleans, 2012.

[6] D. Potter, S. Karl, M. Lambert and K. Hannemann, "Computation of Radiative and Convective Contributions to Viking Afterbody Heating," in *AIAA2013-2895*, San Diego, 2013.

[7] A. M. Brandis, D. A. Saunders, C. O. Johnston, B. A. Cruden and T. R. White, "Radiative Heating on the After-Body of Martian Entry Vehicles," in *AIAA2015-3111*, Dallas, 2015.

[8] S. Gu, R. G. Morgan and T. J. McIntyre, "Study of Afterbody Radiation During Mars Entry in an Expansion Tube," in *AIAA2017-0212*, Grapevine, 2017.

[9] H. Takayanagi, S. Nomura, A. Lemal and K. Fujita, "Measurements of Nonequilibrium Carbon Dioxide Infrared Radiation in an Exapnsion Tube," in *AIAA2017-1369*, Grapevine, 2017.

[10] C. Park, J. T. Howe, R. L. Jaffe and G. J. Candler, "Review of Chemical-Kinetic Problems of Future NASA Missions, II: Mars Entries," *J. Thermophys. Heat Trans.,* vol. 8, pp. 9-23, 1994.

[11] T. C. Clark, A. M. Dean and G. B. Kistiakowsky, "Effect of Organic Impurities on the Observed Activation Energy of CO_2 Dissociation," *J. Chem. Phys.,* vol. 54, pp. 1726-1727, 1970.

[12] A. M. Dean, "Dissociation of Carbon Dioxide Behind Reflected Shock Waves," *J. Chem. Phys.,* vol. 58, pp. 5202-5208, 1973.

[13] W. O. Davies, "Carbon Dioxide Dissociation 6000 to 11,000 K," *J. Chem. Phys.,* vol. 43, pp. 2809-2815, 1965.

[14] M. Burmeister and P. Roth, "ARAS Measurements on the Thermal Decomposition CO_2 Behind Shock Waves," *AIAA J.,* vol. 28, no. 3, pp. 402-405, 1990.

[15] N. Fujii, S. Sagawai, T. Sato, Y. Nosaka and H. Miyama, "Study of the Thermal Dissociation of N_2O and CO_2 using $O(^3P)$ Atomic Resonance Absorption Sepctroscopy," *J. Phys. Chem.,* vol. 93, pp. 5474-5478, 1989.

[16] M. A. Oehlschlaeger, D. F. Davidson, J. B. Jeffries and R. H. Hanson, "Carbon Dioxide Thermal Decomposition: Observation of Incubation," *Z. Phys. Chem.,* vol. 219, pp. 555-567, 2005.

[17] S. Saxena, J. H. Kiefer and R. S. Tranter, "Relaxation, Incubation, and Dissociation in CO_2," *J. Phys. Chem. A,* vol. 111, pp. 3884-3890, 2007.

[18] R. J. Jaffe, "Vibrational and Rotational Excitation and Dissociation of CO_2 Reexamined," *AIAA2011-0447,* 2011.

[19] J. E. Hardy, W. C. Gardiner, Jr. and A. Burcat, "Recombination of Carbon Monoxide and Oxygen Atoms," *Int. J. Chem. Kinetics,* vol. 10, pp. 503-518, 1978.

[20] C. M. Marian, "Spin-Orbit Coupling and Intersystem Crossing in Molecules," *WIREs Comput. Mol. Sci.,* vol. 2, pp. 187-203, 2012.

[21] D. Beijonne, Z. Shuai, G. Pourtois and J. L. Bredas, "Spin-Orbit Coupling and Intersystem Crossing in Conjugated Polymers: A Configuration Interaction Description," *J. Phys. Chem. A,* vol. 105, pp. 3899-3907, 2001.

[22] D. G. Fedorov, S. Koseki, M. W. Schmidt and M. S. Gordon, "Spin-Orbit Coupling in Molecules: Chemistry Beyond the Adiabatic Approximation," *Int. Rev. Phys. Chem.,* vol. 22, pp. 551-592, 2010.

[23] W. R. Wadt, "The Electronic States of Ar^{2+}, Kr^{2+}, Xe^{2+}. I. Potential Curves With and Without Spin-Orbit Coupling," *J. Chem. Phys.,* vol. 68, pp. 402-414, 1978.

[24] J. W. Sidman, "Spin-Orbit Coupling in the $^3A_2$-$^1A_1$ Transition of Formaldehyde," *J. Chem. Phys.,* vol. 29, pp. 644-652, 1958.

[25] C. M. Marian, "Spin-Orbit Coupling in Molecules," in *Reviews in Computational Chemistry, vol. 17*, K. B. Lipkowitz and D. B. Boyd, Eds., New York, Wiley-VCH, 2001, pp. 99-204.

[26] L. D. Landau, "Zur Theorie Der Energieubertragung," *II. Phys. Z. Sowjetunion,* vol. 2, pp. 46-51, 1932.

[27] C. Zener, "Non-adiabatic Crossing of Energy Levels," *Proc. R. Soc. London, Ser. A,* vol. 137, pp. 696-702, 1932.

[28] C. Witting, "The Landau-Zener Formula," *J. Phys. Chem. B,* vol. 109, pp. 8428-8430, 2005.

[29] J. C. Tully, "Molecular Dynamics with Electronic Transitions," *J. Chem. Phys. ,* vol. 93, pp. 1061-

1071, 1990.

[30] B. O. Roos, "The Complete Active Space SCF Method in a Fock-Matrix-Based Super-CI Formulation," *Int. J. Quantum Chem.,* vol. 18, pp. 175-189, 1980.

[31] K. Ruedenberg, M. W. Schmidt, M. M. Gilbert and S. T. Elbert, "Are Atoms Intrinsic to Molecular Electronic Wavefunctions? I. The FORS Model," *J. Chem. Phys.,* vol. 71, pp. 41-49, 1982.

[32] H. -J. Werner and P. J. Knowles, "A Second Order Multiconfiguration SCF Procedure with Optimum Convergence," *J. Chem. Phys. ,* vol. 82, pp. 5053-5063, 1985.

[33] P. J. Knowles and H. -J. Werner, "An Efficient Second-Order MCSCF Method for Long Configuration Expansions," *Chem. Phys. Lett. ,* vol. 115, pp. 259-267, 1985.

[34] H. -J. Werner and P. J. Knowles, "An Efficient Internally Contracted Multiconfiguration Reference Configuration-Interaction Method," *J. Chem. Phys.,* vol. 89, pp. 5803-5814, 1988.

[35] P. J. Knowles and H. -J. Werner, "An Efficient Method for the Evaluation of Coupling Coefficients in Configuration Interaction Calculations," *Chem. Phys. Lett.,* vol. 145, pp. 514-522, 1988.

[36] K. R. Shamasundar, G. Knizia and H. -J. Werner, "A New Internally Contracted Multi-Reference Configuration Interaction Method," *J. Chem. Phys.,* vol. 135, p. 054101, 2011.

[37] H. -J. Werner, P. J. Knowles, G. Knizia, F. R. Manby and M. Schutz, "Molpro: A General Purpose Quantum Chemistry Program Package," *WIREs Comput. Mol. Sci.,* vol. 2, pp. 242-253, 2011.

[38] T. H. Dunning Jr., "Gaussian Basis Sets for Use in Correlated Molecular Calculations. I. The Atoms Boron through Neon and Hydrogen," *J. Chem. Phys.,* vol. 90, pp. 1007-1023, 1989.

[39] D.-Y. Hwang and A. M. Mabel, "Ab initio Study of Spin-forbidden Unimolecular Decomposition of Carbon Dioxide," *Chem. Phys.,* vol. 256, pp. 169-176, 2000.

[40] A. Berning, M. Schweizer, H. -J. Werner, P. J. Knowles and P. Palmieri, "Spin-Orbit Matrix Elements for Internally Contracted Multireference Configuration Interaction Wavefunctions," *Mol. Phys.,* vol. 98, pp. 1823-1833, 2000.

[41] D. W. Schwenke, R. L. Jaffe and G. Chaban, "Collisional Dissociation of CO: ab initio Potential Energy Surfaces and Quasiclassical Trajectory Rate Coefficients," *submitted to J. Phys. Chem. .*

[42] X. Huang, D. W. Schwenke, S. Tashkun and T. J. Lee, "An Isotopic-Independent Highly Accurate Potential Energy Surface for CO_2 Isotopologues and an Initial $^{12}C^{16}O_2$ Infrared Linelist," *J. Chem. Phys.,* vol. 135, pp. 124311-17, 2012.

[43] D. W. Schwenke, "unpublished".

[44] https://www.nist.gov/pml/atomic-spectral-database.

[45] D. W. Schwenke, "Calculations of Rate Constants for the Three-Body Recombination of H_2 in the Presence of H_2," *J. Chem. Phys.,* vol. 89, pp. 2076-2091, 1988.

[46] G. Granucci and M. Persico, "Critical Appraisal of the Fewest Switches Algorithm for Surface Hopping," *J. Chem. Phys. ,* vol. 126, p. 134114, 2007.

[47] W. H. Press, S. A. Teukolsky, W. T. Vettering and B. P. Flannery, Numerical Recipes in Fortran, 2nd ed., Cambridge Univesity Press, 1992, p. 270.

[48] R. L. Jaffe, D. W. Schwenke and M. Panesi, "First Principles Calculation of Heavy Particle Rate Coefficients," in *Hypersonic Nonequilibrium Flows: Fundamentals and Recent Advances*, vol. 247, E. Josyula, Ed., Reston, AIAA, 2015, pp. 103-158.

[49] C. W. Eaker and D. W. Schwenke, "A Fast Fourier Transform Method for the Quasiclassical Selection of Initial Rovibrational States of Triatomic Molecules," *J. Chem. phys.,* vol. 103, pp. 6984-6992, 1995.

[50] D. W. Schwenke, "Variational Calcuations of Rovibrational Energy Levels and Transition Intensities for Tetratomic Molecules," *J. Phys. Chem.,* vol. 100, pp. 2867-2884, 1996.

[51] D. W. Schwenke, "A Theoretical Prediction of Hydrogen Molecule Dissociation-recombination Rates including an Accurate Treatment of Internal State Nonequilibrium Effects," *J. Chem. Phys.,* vol. 92, pp. 7267-7282, 1990.

21